

Algorithm Description Document for Version 4.2 of the Three-Dimensional Gridded NEXRAD WSR-88D Radar (GridRad) Dataset

Last Revised: 10 January 2023

Revision History:

- 3 February 2022 - Original release.
- 10 January 2023 - Revised Figs. 10 & 11.

Author Information:

Cameron R. Homeyer*
School of Meteorology
University of Oklahoma
Norman, OK 73072-7307
Contact: chomeyer@ou.edu

Kenneth P. Bowman
Department of Atmospheric Sciences
Texas A&M University
College Station, TX 77843-3150
Contact: k-bowman@tamu.edu

*Primary scientific contact.

Table of Contents

1	Introduction	3
1.1	Objective	3
1.2	Scope	3
1.3	Executive Summary for GridRad v3.1 Users	3
2	NEXRAD WSR-88D Data	4
3	GridRad Algorithm	7
3.1	Overview	7
3.2	Procedure	7
3.3	Merging of the Polarimetric Variables	10
3.4	Merging of the Kinematic Variables	11
4	Data Quality	14
4.1	Resolution	14
4.2	Limitations	16
5	Example Code and GridRad Data Usage	19
5.1	Recommendations	19
5.2	GridRad Examples of Common Radar Analyses	21
6	Table of Symbols	26
7	References Cited	27

1 Introduction

1.1 Objective

The objective of this document is to describe the algorithms used to produce Version 4.2 of the three-dimensional Gridded NEXRAD WSR-88D Radar data. This data set is referred to as *GridRad*. Additional information is available at [GridRad.org](https://gridrad.org). Two collections of v4.2 GridRad data are available for download from the Research Data Archive of the National Center for Atmospheric Research: an hourly archive of warm-season data (April through August) for 2008 – 2021 ([ds841.1](#)) and an archive of selected severe weather events from 2010 – 2021 (GridRad-Severe; [ds841.6](#)).

1.2 Scope

The scope of this document is a detailed outline of the characteristics of NEXRAD WSR-88D Level 2 (i.e., native volume scan) data, the computational steps used to merge Level 2 data onto large-area grids, and recommended use of the GridRad data produced by these methods. Individuals may leverage the detail within this document to reproduce the GridRad methods or reference it when analyzing the publicly available dataset to ensure proper scientific understanding and evaluation. Example code for reading and quality-controlling GridRad data is also provided.

1.3 Executive Summary for GridRad v3.1 Users

Users of v3.1 data who have reviewed the corresponding Algorithm Description Document in detail will want to focus attention on §3.3 and §3.4 of this document for the most significant algorithm differences in v4.2. For convenience, the following list is a summary of key changes from v3.1 to v4.2:

- The analysis domain now extends from 125°W to 66°W longitude and 24°N to 50°N latitude, which includes all of the contiguous United States.
- The horizontal grid has been changed from 50 points per degree longitude-latitude (0.02° spacing) in v3.1 to 48 points per degree ($\sim 0.02083^\circ$) in v4.2. This change allows for more flexible area-averaging of the data for statistical analysis and has negligible impact on the level of detail captured in the GridRad data.
- The vertical grid resolution in the lowest 7 km of the GridRad volumes has been increased from 1 to 0.5 km. The top of the volumes has been reduced from 24 to 22 km. As a result, the total number of vertical levels has increased from 24 to 29.
- All Level 2 volumes are interpolated (if necessary) to a standard polar grid prior to binning onto the GridRad Cartesian grid. The standard grid has an azimuthal grid spacing of 0.5° and a range/radial grid spacing of 0.25 km, which is the highest-resolution Level 2 grid available for the current period of record.
- The maximum time difference from the GridRad analysis time allowed for binning was increased slightly from ± 3.8 min to ± 5 min. No change has been made to the weighting function used for binning.
- A list of individual elevation scans from each contributing radar is contained in the v4.2 GridRad files rather than the names of entire Level 2 volumes.
- In addition to the radar reflectivity at horizontal polarization, the radial velocity spectrum width is included in all GridRad v4.2 files. Additional kinematic variables (based on radial velocity) and dual-polarization variables are included in the GridRad-Severe data.
- The recommended quality control techniques have been simplified.

2 NEXRAD WSR-88D Data

The U.S. operational weather radar system, now known as the Next Generation Weather Radar (NEXRAD) program, was created in 1957. Beginning in 1988, the network was upgraded to Doppler S-band (10–11.1 cm wavelength) horizontal-polarization radars (Weather Surveillance Radar 1988 Doppler or WSR-88D) to measure the radial velocity V_R and the velocity spectrum width σ_V in addition to the radar reflectivity factor Z_H (Crum and Alberty, 1993). From 2011 to 2013, the WSR-88D systems were further upgraded to obtain measurements at both horizontal (H) and vertical (V) polarization. The added dual-polarization (polarimetric) variables are the differential radar reflectivity Z_{DR} , the differential propagation phase shift ϕ_{DP} , and the co-polar correlation coefficient ρ_{HV} . The polarimetric variables provide information on the size, shape, and concentration of hydrometeors. There are now 143 operational WSR-88D radars in the contiguous U.S. (CONUS) providing nearly continuous coverage of storm systems and their microphysical characteristics. Figure 1 shows the locations of these radars and their combined coverage at the lowest scanned altitudes.

Data from operational NEXRAD WSR-88D radars are archived at the National Centers for Environmental Information (NCEI, formerly the National Climatic Data Center) and Amazon Web Services (AWS) for the period from 5 June 1991 to the present, although data availability for most current systems in the network begins in 1995. The archives include the native three-dimensional data from each radar system (Level 2 data), which are provided on a spherical grid (azimuth, elevation, and range) with its origin at the radar location. Observations from individual systems are subject to some outages and interruptions, but these are typically limited to a few days each year. In general, data gaps are more frequent during years prior to 2005 (see Fig. 3 in Homeyer and Bowman, 2021).

The resolution of each radar observation depends on the operating mode (meteorological target) and year. In particular, the number of elevation angles in a volume can be as high as 14 for convection and as low as 5 for clear air or shallow precipitating systems. Select combinations of elevation angles are referred to as Volume Coverage Patterns (VCPs), with each unique VCP accompanied by a number code. Convection is typically sampled using VCP-11 or VCP-12 (or one of their derivatives), both of which contain 14 elevation angles and, in recent years, repeated scans of the lowest few elevations during each volume to provide more rapid updates of storms and related hazards. VCP-12 is often the preferred VCP for convection in recent years. Winter storms (or other shallow precipitation) are typically sampled using VCP-21 (or one of its derivatives), which contains 9 elevation angles. The elevation angles typical of these three VCPs are provided in Table 1. For more information on NEXRAD scanning strategies and characteristics, the reader is directed to Part C of the Office of the Federal Coordinator for Meteorology (OFCM) Federal Meteorological Handbook No. 11 (OFCM, 2006).

Operating Mode	Elevation angles (°)
VCP-11	0.50, 1.45, 2.40, 3.35, 4.30, 5.25, 6.20, 7.50, 8.70, 10.0, 12.0, 14.0, 16.7, 19.5
VCP-12	0.50, 0.90, 1.30, 1.80, 2.40, 3.10, 4.00, 5.10, 6.40, 8.00, 10.0, 12.5, 15.6, 19.5
VCP-21	0.50, 1.45, 2.40, 3.35, 4.30, 6.00, 9.00, 14.6, 19.5

Table 1: Elevation angles of the three most common VCPs employed when NEXRAD WSR-88D radars sample precipitation: VCP-11, VCP-12, and VCP-21.

Data storage requirements for NEXRAD data have changed over time due to changes in the spatial grid resolution and the introduction of new measurement variables. Data from the period prior to May of 2008 are stored at an azimuthal resolution of 1° and a range resolution of 1 km. Beginning in May of 2008 the

NEXRAD Coverage Below 10,000 Feet AGL

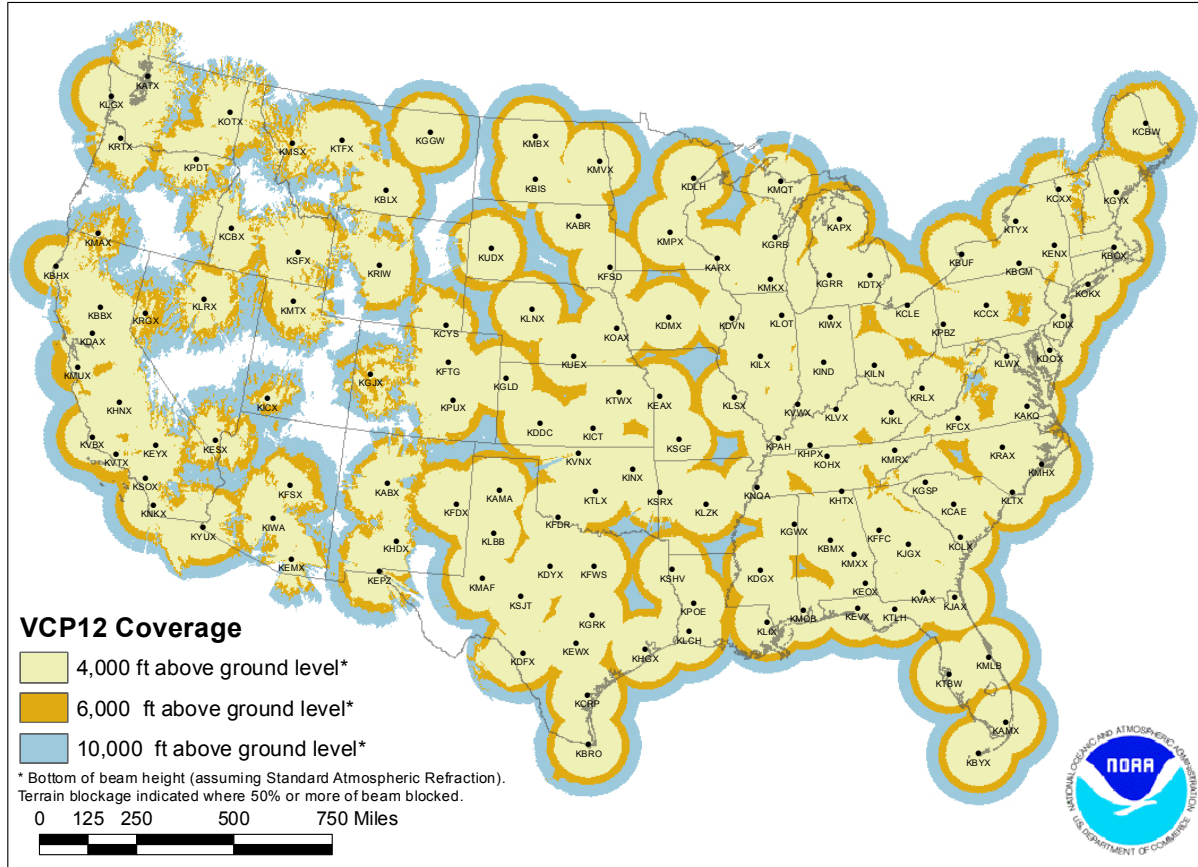


Figure 1: Map of NEXRAD WSR-88D radars within the CONUS and their lowest sampled altitudes for only those altitudes less than 10,000 ft AGL (~3 km). Credit: NOAA, available online at <https://www.roc.noaa.gov/WSR88D/Maps.aspx>.

radars transitioned to a range resolution of 250 m and an azimuthal resolution of 0.5° for the lowest 3-5 elevations (referred to as “super-resolution”). The addition of polarimetric variables has also increased the volume of archived data. A single WSR-88D volume scan of deep convection prior to 2008 includes only three variables (Z_H , V_R , and σ_V) on the coarser spherical grid ($1 \text{ deg} \times 1 \text{ km} \times 14$ elevations) and has a file size of ~15 MB. In comparison, a similar current observation with the additional polarimetric variables (Z_{DR} , ϕ_{DP} , and ρ_{HV}) on the higher-resolution spherical grid has a file size of ~45 MB, which is a factor of 3 larger than the earlier files. As a result of the large data volume, data storage and handling is a significant challenge for studies of longer periods. For example, the entire Level 2 archive includes 160 radars and requires ~55 TB of data storage per year for recent years (<https://www.ncdc.noaa.gov/nexradinv/stats.jsp>).

Several previous efforts in addition to v3.1 of GridRad have attempted to improve the utility of NEXRAD data by merging observations from multiple radars onto three-dimensional Earth-referenced grids (typically longitude, latitude, and altitude; hereafter ‘gridded’ data), including the NOAA MRMS and related MYRORSS activities. This can reduce storage requirements and make the data easier to use. The overlapping observations from multiple NEXRAD WSR-88D radars also allow for a three-fold increase in vertical sam-

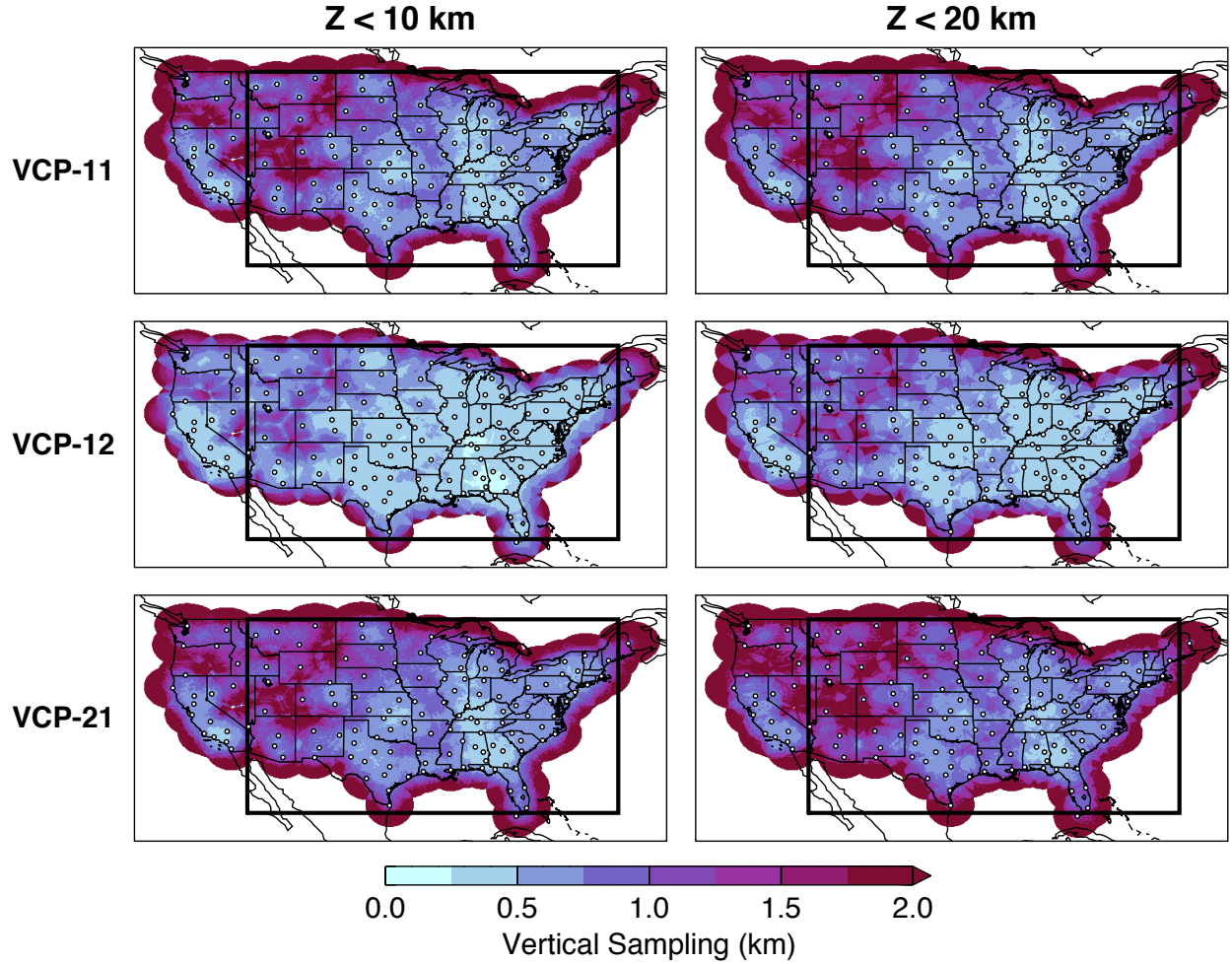


Figure 2: Maps of the combined vertical sampling of merged radar volumes using data out to 300 km in range from radars within the NEXRAD WSR-88D network. The left and right columns show average vertical sampling within the 0-10 km and 0-20 km AMSL altitude layers, respectively. Vertical sampling is computed assuming all contributing radars are operating in (top) VCP-11, (middle) VCP-12, and (bottom) VCP-21. The locations of individual radars (white dots) and the GridRad domain (thick black box) are superimposed.

pling compared to an individual radar (i.e., the vertical resolution Δz can be increased from 3 km on average to less than 1 km), which provides an important improvement in the utility of NEXRAD data for research. For example, Figure 2 shows the combined vertical sampling in altitude layers of 0-10 km and 0-20 km AMSL from merging of NEXRAD WSR-88D Level 2 data assuming individual radars are operating in each of the three typical VCPs, as outlined above. These improvements in the utility of NEXRAD data through multi-radar merging motivate the development of the GridRad dataset. The following section outlines the methods employed to create GridRad data.

3 GridRad Algorithm

3.1 Overview

Merging individual NEXRAD WSR-88D volumes onto a common large-area grid can be a somewhat complicated process that depends on the radar variable being merged and its intended use when complete. Established alternative approaches to that outlined here exist, such as those employed in the Multi-Radar, Multi-Sensor (MRMS) system produced operationally within the NOAA National Severe Storms Laboratory (NSSL). This section is meant to outline the common steps for merging any radar variable in the GridRad dataset and additional steps for radar variables that require unique treatment during one or more of the common steps of the process.

In the following we distinguish between the observations from a single radar, which are made on a spherical polar coordinate grid with the radar located at the origin, and the GridRad data, which are defined on a regular longitude-latitude-altitude grid. A *Level 2 radar volume* is an observation made by a single radar at a given azimuth, elevation, and range or ‘gate’. A *GridRad volume* is a rectangular volume in longitude, latitude, and altitude¹. The GridRad analysis domain extends from 235°E to 294°E (125°W to 66°W) longitude, 24°N to 50°N latitude, and 0.5² to 22 km in altitude above mean sea level (AMSL). The grid resolution is 48 grid points per degree of longitude or latitude ($\sim 0.02083^\circ$) and 0.5 or 1 km in altitude. For the latitude range of the analysis domain, the physical size of the grid boxes is $\sim 1.5 \text{ km} \times \sim 2 \text{ km} \times 0.5$ or 1 km. The altitude grid spacing is 0.5 km in the lowest 7 km AMSL and 1 km above. The centers of the GridRad volumes (x_i, y_j, z_k) are given by

$$\begin{aligned} x_i &= x_0 + (i + 0.5) \cdot \delta x, & i &= 0, \dots, N_x - 1 \\ y_j &= y_0 + (j + 0.5) \cdot \delta y, & j &= 0, \dots, N_y - 1 \\ z_k &= 0.5, \dots, 7.0, 8.0, \dots, 22.0, & k &= 0, \dots, 13, 14, \dots, 28 \end{aligned} \quad (1)$$

where x_i is longitude in degrees east, $\delta x = \delta y = 1^\circ/48$, y_j is latitude in degrees north, and z_k is altitude in km. The full CONUS GridRad grid has $x_0 = 235^\circ\text{E}$, $N_x = 2832$, $y_0 = 24^\circ\text{N}$, and $N_y = 1248$ (~ 102.5 million grid volumes). For any given analysis a large majority of the grid volumes have no observable radar echo. To reduce the storage space required, a sparse storage scheme is used (see §5).

The GridRad algorithm is a four-dimensional binning (averaging) procedure that merges multiple Level 2 radar volumes to estimate radar variables within the GridRad volumes at a desired analysis time (typically at 5-min or hourly intervals). The Level 2 observations are weighted by their distance from the radar and by the time difference between the observation and analysis time.

3.2 Procedure

Creation of GridRad data follows a 4-step procedure that is repeated for each contributing Level 2 volume:

1. Read NEXRAD WSR-88D Level 2 observation in polar coordinates (i.e., azimuth, elevation, and range relative to the radar location).
2. Identify common GridRad volumes in which to bin the Level 2 observations.
3. Compute space-time weights of each Level 2 grid volume.

¹Technically the GridRad volumes are defined in Earth-centered spherical polar coordinates. Because the dimensions of a grid box are small compared to the radius of the Earth, the individual grid volumes are effectively rectangular.

²The lowest altitude in the v4.2 hourly GridRad archive is 1 km.

4. Compute weighted averages of radar variable(s) for all GridRad bins with valid data.

Note: Steps 2-4 are carried out for each azimuthal sweep (i.e., 360° scan at a single elevation) of a Level 2 volume and Step 4 is repeated for an azimuthal sweep when more than one radar variable is binned into the common grid (e.g., Z_H and the polarimetric variable Z_{DR}). Each step is outlined in the following paragraphs.

Step 1. Read NEXRAD WSR-88D Level 2 observation in polar coordinates.

As outlined in §2, the characteristics of the NEXRAD WSR-88D Level 2 data have changed over time, including the resolution of the polar grid, the scan strategy (i.e., vertical sampling), and the radar variables observed. These changes affect the quality of the data beyond that due to the pulse frequency and power of the radar beam, which are often the most important elements to consider when merging multiple radars of the same wavelength onto a common grid. In particular, the maximum unambiguous range of a NEXRAD WSR-88D radar depends on the variable observed and transmitted pulse repetition frequency. V_R and σ_V are only observed out to 230 km in range in the older, lower resolution Level 2 data and out to 300 km in range in the more recent, higher resolution volume scans (i.e., since mid-2008). On the other hand, Z_H is observed out to 460 km in range throughout time. The polarimetric variables (Z_{DR} , ϕ_{DP} , and ρ_{HV}), available from all NEXRAD WSR-88D radars since early 2013, are observed out to 300 km in range.

Considering the above limitations of NEXRAD WSR-88D sampling and the goal of a merged dataset to improve spatial coverage from the overlapping of neighboring radars, only observations out to 300 km in range from each radar and within 5 min of the analysis time are merged by the GridRad procedure. The time limit is imposed to prevent excessive smoothing of GridRad data due to time averaging. In addition, because the space and time resolution of the Level 2 spherical grids (and ultimately, the number of gates that can be merged) varies over time, all volumes are linearly interpolated (if necessary) to a common polar grid with an azimuthal spacing of 0.5° and a range spacing of 250 m upon reading. The longitude, latitude, and altitude relative to the geoid are computed for each Level 2 radar volume using simple geometry that accounts for the spherical shape of the Earth and assumes the standard index of refraction for the atmosphere in the vertical (e.g., see Chapter 2 in [Doviak and Zrnić, 1993](#)). The central time of each azimuthal sweep is used for binning purposes (azimuthal sweeps are typically completed in ~ 20 s by NEXRAD radars when sampling precipitation). To ensure that all usable data are included, Level 2 volume scans within ± 10 min of the GridRad analysis time are examined for azimuthal sweeps that fall within the ± 5 min time window.

Step 2. Identify Level 2 radar volumes that contribute to each common grid volume.

The Earth-referenced coordinates computed in Step 1 are used to find the radar volumes that contribute to each GridRad grid volume. Because the NEXRAD WSR-88D beam is conical, with an average angular beam width of 0.95° , the volume observed by the radar increases with range. In the horizontal, Level 2 radar volumes are assumed to contribute only to the nearest GridRad column. In altitude, each Level 2 radar volume may contribute to more than one GridRad volume, depending on range from the radar. The beam width is taken to be the full width at half maximum of the transmitted beam power. Thus, despite the increasing size of the radar beam with increasing range, the majority of the returned power comes from targets near the beam center (e.g., a collection of precipitation-sized hydrometeors). This results in relatively small differences in the radar variables when measured at small and large distances from a radar, as long as the scatterers are somewhat homogeneous within the field of view (e.g., see Figure 5 in [Homeyer \(2014\)](#)). Nevertheless, it is not appropriate to treat observations made at significantly different ranges from a radar equivalently when merging data onto a common grid. While this treatment is primarily handled through weighting of the individual Level 2 radar volumes in space and time (see Step 3 below), we also set an

upper limit to altitude assignments of the beam in the averaging procedure. In particular, we do not allow an individual Level 2 radar volume to contribute to a depth larger than 0.75 km at altitudes below 7 km AMSL and a depth larger than 1.5 km aloft (up to three 1-km grid volumes). This limit reduces the potential contribution of radar observations beyond a range of ~ 40 (~ 90) km (i.e., the point at which the NEXRAD WSR-88D beam depth – and similarly, width – reaches 0.75 (1.5) km; see Fig. 4 below). This restriction prevents excessive smoothing of the GridRad data from observations made at large ranges, which can lead to both the loss of important detail from contributing observations at smaller ranges from a radar and an exaggeration of the spatial extent of echo. One result of this restriction is that ring-shaped sampling artifacts are visible in the gridded data at larger ranges (i.e., where radar conical scans intersect horizontal GridRad surfaces), but this is unavoidable due to the resolution and sampling strategies of the radars.

Step 3. Compute space-time weights of each Level 2 polar grid volume.

The approach of distance-weighting has been explored in previous studies that merge individual radar volumes onto a common grid and is used primarily to retain spatial scales that are adequately sampled from one radar while preventing retention of corresponding observations from additional radars that are under-sampled (e.g., [Trapp and Doswell, 2000](#); [Zhang et al., 2005](#); [Langston et al., 2007](#)). The GridRad algorithm uses Gaussian weighting in space and time. The weight w is

$$w(r, t) = e^{-r^2/L^2} e^{-\Delta t^2/\tau^2}, \quad (2)$$

where r is the radial distance of the polar grid volume (3D slant range) from the radar location in kilometers, $L = 150$ km is the spatial scale, Δt is the time difference between the azimuthal-scan time and GridRad analysis time in seconds, and $\tau = 150$ s is the time scale. Figure 3 shows this weighting function out to 300 km in range from a radar and 300 s in time from the GridRad analysis. Sensitivity tests (not shown) demonstrate that changes in the internal microphysical characteristics of a storm from varying L or τ are minimal for values less than 150 km (or s), while values significantly greater than these thresholds show much less detail (i.e., excessive smoothing).

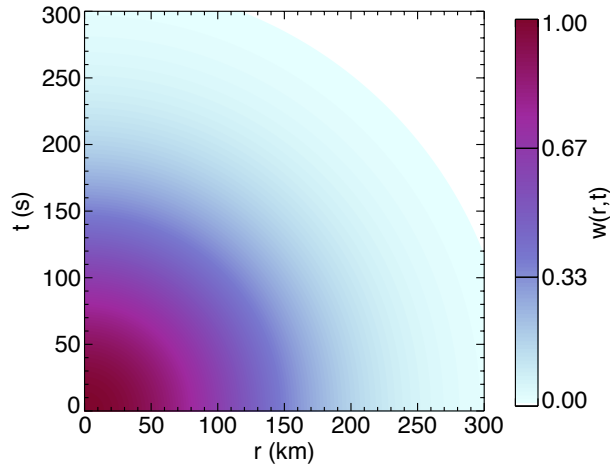


Figure 3: Contour plot of the space-time weighting applied to NEXRAD WSR-88D Level 2 observations in the GridRad binning procedure.

Step 4. Bin radar variable(s) scaled by space-time weights into common grid.

The final step of the GridRad algorithm involves merging multiple observations of a given radar variable into the common grid volumes (i.e., ‘bins’) of the GridRad domain. In the Level 2 data, each radar volume on the polar grid is flagged to indicate whether a valid measurement was made and whether echo was detected. The value of a radar variable V on the GridRad grid is equal to the weighted average of all observations in which echo was detected

$$V(x_i, y_j, z_k) = \frac{\sum_{n=1}^{N_{\text{echo}}} w_n v_n}{\sum_{n=1}^{N_{\text{echo}}} w_n}, \quad (3)$$

where N_{echo} is the number of Level 2 radar volumes with echo that contribute to the grid volume at location (x_i, y_j, z_k) , $w_n = w(r_n, t_n)$ is the space-time weight of the n th Level 2 radar volume on its polar grid (from Equation 2 and Figure 3 above), and v_n is the value of the observed radar variable for the n th Level 2 radar volume. The total weight W is

$$W(x_i, y_j, z_k) = \sum_{n=1}^{N_{\text{echo}}} w_n. \quad (4)$$

Thus the GridRad data are averages conditioned on whether echo is observed. Though generally advantageous for all radar variables, this space-time weighting approach is especially beneficial for estimating polarimetric variables, which can be significantly degraded at far ranges where the minimum detectable Z_H increases and the signal-to-noise ratio becomes small. Prescribing less weight to distant scans with potentially degraded data quality mitigates possible detrimental effects on the resulting GridRad analysis.

The result of the binning process is two parameters for each radar variable: the weighted average V (e.g., Z_H) and the sum of the weights W . Two additional parameters that are useful for post-processing quality control are also archived: N_{obs} , which is the number of valid Level 2 radar volumes that observed each GridRad volume (with or without echo), and N_{echo} . W is also useful for quality control as it represents a measure of the intrinsic resolution and/or sampling within a given GridRad volume. The sum weight W indicative of a well-sampled v4.2 GridRad volume is ~ 1.5 .

3.3 Merging of the Polarimetric Variables

When the polarimetric variables Z_{DR} , ϕ_{DP} , and ρ_{HV} are routinely available (i.e., 2013 to the present), they can be merged into the GridRad volumes. At present, the only public v4.2 dataset that includes polarimetric variables is the GridRad-Severe archive. Merging of the polarimetric variables requires some unique procedures during the common 4-step GridRad procedure, which are outlined in this section. First, since ϕ_{DP} is a measure of the cumulative relative phase shifting of the H and V beams as they propagate away from and back to the radar, measurements of ϕ_{DP} at a particular location from radars with different viewing paths are fundamentally different quantities. The local contribution to ϕ_{DP} is estimated from the specific differential phase, defined as:

$$K_{\text{DP}} = \frac{1}{2} \frac{\partial \phi_{\text{DP}}}{\partial r}. \quad (5)$$

One important limitation of K_{DP} , however, is that instantaneous observations can suffer from a considerable amount of random noise, particularly in light rain or ice. Despite this limitation, studies have shown that time and space averaging of K_{DP} (an intrinsic property of the GridRad binning method) largely removes this noise and provides some of the most accurate radar-derived estimations of precipitation (e.g., [Ryzhkov et al., 2005b](#); [Borowska et al., 2011](#)).

K_{DP} fields can be noisy, due in part to calculating the derivative of an already noisy variable. The problem is largest when small radial path lengths are used or ϕ_{DP} is not smoothed before computing the range derivative. In the GridRad procedure, noise in ϕ_{DP} is reduced through application of a 7.5-km radial running-mean (boxcar) filter. The radially smoothed ϕ_{DP} fields are then used to compute K_{DP} using centered differencing at each 0.25-km radar gate. These K_{DP} values are then merged into the GridRad analysis using the common 4-step method.

The second polarimetric variable that requires special treatment is Z_{DR} . Systematic biases in Z_{DR} (i.e., those resulting from inadequate radar maintenance and calibration) are unfortunately common in the NEXRAD WSR-88D observations (e.g. [Cunningham et al., 2013](#); [Homeyer and Kumjian, 2015](#)). These biases can introduce unphysical variations and/or offsets in the GridRad output that adversely affect analyses of the data. In order to create useful Z_{DR} volumes, an approach for bias correction must be employed prior to Step 4 of the GridRad procedure. Following that outlined in detail in [Homeyer and Kumjian \(2015\)](#), GridRad uses an objective natural scatterer approach (e.g., [Ryzhkov et al., 2005a](#); [Melnikov et al., 2011, 2013](#)). While the preferred approach for bias correction in polarimetric radar observations is a so-called “engineering method” (see [Melnikov et al. \(2003\)](#) for an outline of the ideal NEXRAD WSR-88D approach), such a method can only be carried out if information on the performance of all components of the radar is available (i.e., transmitted power, gain, and noise in the H and V polarized beams). Such information is not archived in the Level 2 volumes, so a natural scatterer method (or a similar approach) must be used instead.

In the GridRad procedure, Z_{DR} bias correction is performed for each Level 2 volume immediately prior to Step 4 of the common procedure. In particular, gates in each Level 2 volume lying above the environmental freezing (i.e., 0°C) level with Z_H values ranging from 20 to 30 dBZ and ρ_{HV} values greater than 0.95 (to isolate snow aggregates) are found and the median Z_{DR} of these gates is compared to a value of 0.36 dB. The difference between the median Z_{DR} of the gate sample and the reference value of 0.36 dB is then assumed as the bias for correcting Z_{DR} throughout the Level 2 volume. The 0.36 dB reference value is based on an analysis of a small sample of NEXRAD WSR-88D observations that were corrected using engineering methods (see extended discussion and presentation in [Homeyer and Kumjian \(2015\)](#)). Archived v4.2 GridRad data uses hourly freezing level heights from the ERA5 reanalysis for reference during Z_{DR} bias correction ([10.24381/cds.adbb2d47](#)), which are linearly interpolated in space and time to each radar observation.

3.4 Merging of the Kinematic Variables

As outlined in §2, the kinematic variables radial velocity V_R and velocity spectrum width σ_V have always been measured by the NEXRAD WSR-88D radars, though they are observed at farther ranges since mid-2008. These variables provide valuable additional information for the analysis of storms, especially those producing severe and/or hazardous weather. However, there are some unique challenges to merging such data (particularly V_R) onto a common grid. The single biggest challenge is that V_R is a measure of the motion of precipitation-sized particles toward and away from the radar, such that any given measurement has a unique geometry and thus is not directly comparable to a measurement made at the same location from

a different radar (similar to the dilemma for ϕ_{DP} outlined in §3.3). Thus, merging of information contained in V_R is not a simple process. In GridRad, we instead merge two derivatives of V_R : 1) the azimuthal derivative (azimuthal shear) and 2) the radial divergence (where the leading component is the radial derivative). Multiple quality control steps are undertaken prior to computing the derivatives for merging during Step 1 of the GridRad procedure, outlined extensively in [Sandmæl et al. \(2019\)](#) and summarized briefly below.

First, since V_R is prone to large errors in magnitude and sign due to aliasing (i.e., winds that exceed the maximum detectable V_R at a given operating frequency – the Nyquist velocity – and become “folded”), they must be de-aliased prior to computing the derivatives. In order to accomplish this necessary quality control step, we employ the Python ARM Radar Toolkit (Py-ART; [Helmus and Collis, 2016](#)). Py-ART provides multiple de-aliasing techniques, some that require a reference atmospheric wind profile and others that do not. For use in GridRad, we invoke a Py-ART routine that does not require a reference atmospheric wind profile and is computationally more efficient than alternative approaches – `dealias_region_based` – which accomplishes de-aliasing by modeling the problem as a dynamic network reduction.

Following de-aliasing, random fluctuations of V_R in each azimuthal sweep are further suppressed using a 3x3 median filter and a 5-gate running-mean (boxcar) range filter prior to computing derivatives (in that order). As with K_{DP} , centered differencing is employed to compute azimuthal shear and radial divergence. While the scales for differencing are constant in range for each Level 2 volume, the spatial resolution of azimuthal sampling is not. Thus, azimuthal shear is computed at a changing spatial resolution with range. Figure 4 demonstrates this characteristic for azimuthal sweeps with 0.5 and 1.0 degree sampling, where azimuthal shear (a partial measure of vertical vorticity, or rotation) is resolved at a scale of twice this sampling resolution. Though it is possible to apply an adjustment to azimuthal shear to account for changing spatial resolution with range (if a characteristic diameter circulation is assumed), the GridRad procedure does not include such an adjustment but, rather, leaves emphasis of scaling to the space-time weight each observation carries in the common gridded volume. The expected worst-case uncertainty of azimuthal shear and radial divergence calculations is 0.004 s^{-1} (though typically much smaller) and the minimum resolvable scales of circulations (vortices) range from 2-6 km. It is worth reiterating here that all NEXRAD Level 2 observations are placed on a common polar grid with 0.5° azimuthal and 0.25-km radial grid spacing prior to being ingested into the v4.2 GridRad binning procedure, which helps mitigate some of the coarsening of V_R information during derivative calculation.

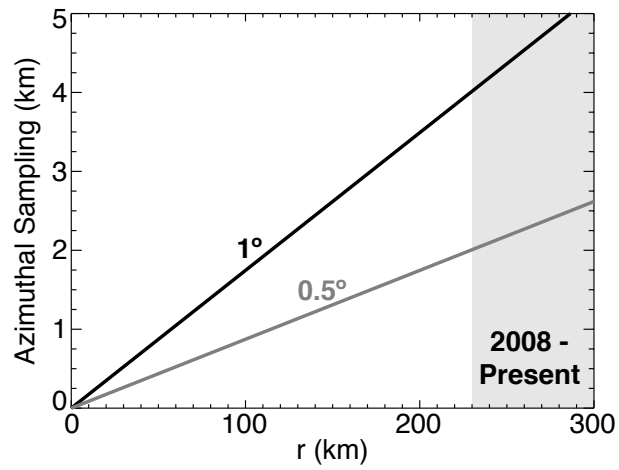


Figure 4: Azimuthal sampling (in km) as a function of range for NEXRAD WSR-88D scans taken at 1° (thick black line) and 0.5° (thick gray line) intervals. The light gray color-filled portion of the range represents the added information available in Level 2 volumes following the upgrade to super-resolution in 2008. Note: the azimuthal sampling for sweeps with 1° intervals shown here is nearly equivalent to the beam width/depth as a function of range (i.e., the gate resolution) given that the average beamwidth of a NEXRAD WSR-88D radar is 0.95° .

4 Data Quality

The gridded radar variables output by the GridRad procedure have some intrinsic characteristics and limitations set by the original scales of the contributing NEXRAD WSR-88D Level 2 gates, the availability of data, common artifacts present in the observations, and the gridding procedure employed. For brevity, an outline of the expected resolution of the data and a description of the most common sources of error are provided in the following subsections.

4.1 Resolution

As discussed at various points in §2 & §3 above, individual grid volumes (or gates) in NEXRAD Level 2 data exist at a resolution of $\Delta r \times \ell(r)^2$, where $\ell(r)$ is the beam width/depth as a function of range. For observations that carry the vast majority of weight in GridRad output (i.e., see Fig. 3), these grid volumes are $1 \text{ km} \times (\leq 3)^2 \text{ km}^2$ in observations prior to 2008 and $0.25 \text{ km} \times (\leq 3)^2 \text{ km}^2$ in observations following the super-resolution upgrade. Though the finer horizontal dimension of the observations is $\leq 1 \text{ km}$, the process of merging involves collecting data from multiple viewing angles at a point and averaging them together. Such a process leads to a loss of information at the finest resolved scales (i.e., smoothing), a reduction in noise (error), and a mean resolution similar to the larger dimension of the Level 2 radar volume (for NEXRAD WSR-88D observations this is the cross-beam dimension $\ell(r)$, except when r is small). The potential loss of information is one of the main motivating factors for applying distance-weighting to contributing observations in a multi-radar dataset. Weighting observations from nearby radars higher than those from distant radars preserves the higher resolution data. Given the rapid decrease in space-time weight as a function of range applied to Level 2 gates in the GridRad procedure, the gridded radar variables produced are expected to have an average horizontal resolution similar to the common grid spacing: $\sim 2 \text{ km}$.

Vertical resolution of GridRad data is primarily influenced by two factors: 1) the combined vertical sampling from neighboring radars, and 2) the beam depth $\ell(r)$. The combined vertical sampling and coverage within the NEXRAD WSR-88D network is greatest (typically ~ 0.5 to 1 km , depending on the VCP of contributing radars; see Fig. 2) where the mean range of a grid point from contributing radars is $\sim 130 \text{ km}$, which corresponds to an average beam depth of $\sim 2 \text{ km}$. As a result, the combined vertical sampling from multiple radars typically exceeds the native resolution of Level 2 gates by a factor of two or more. Given this characteristic and the strict 0.75 or 1.5 km contributing depth limit of a Level 2 gate in Step 2 of the GridRad procedure, the gridded radar variables produced are expected to have an average vertical resolution of $1\text{-}2 \text{ km}$, also similar to the vertical spacing of the common grid.

To better demonstrate these expected resolutions of the GridRad data, two example data comparisons with observations from similar systems made at finer spatiotemporal resolution are provided here. For both comparisons, the GridRad data have been quality controlled using the *filtering* method outlined in §5.1. First, a comparison with 1-minute observations taken by a vertically pointing S-band radar operated during the Midlatitude Continental Convective Clouds Experiment is shown (MC3E; Jensen et al., 2016). Four NEXRAD radars contribute to the GridRad data at the location of the MC3E radar, made at distances of about $60, 120, 140, 180 \text{ km}$ from their locations. Figure 5 shows vertical time curtains of Z_H from the MC3E observations and from GridRad data made at 1-min frequency over a time period of 17.5 hours. The MC3E data are shown i) in their native form (an altitude resolution Δz of 62.5 m ; Fig. 5a) and ii) following altitude (1.125-km running mean) and time ($\pm 5\text{-min}$ Gaussian) smoothing in an effort to mimic the GridRad binning procedure (Fig. 5c). Note that there are some scanning artifacts at and above the echo top in the MC3E data, mostly prior to 400 minutes past 00:00 UTC. This comparison reveals two important characteristics of the GridRad data. First, the finer vertical resolution of the MC3E data is clear, with the Z_H maximum coincident

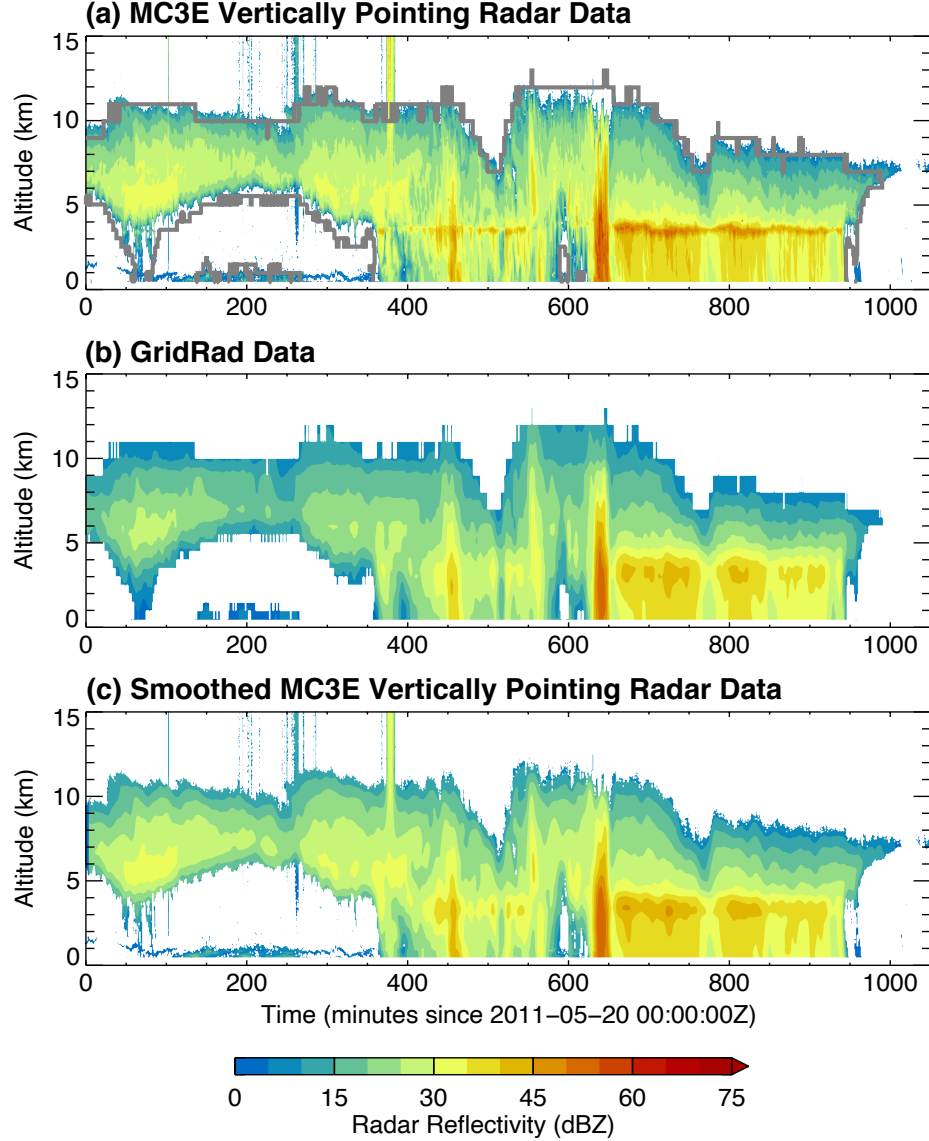


Figure 5: Vertical time curtains of Z_H from (a) a vertically pointing S-band Doppler radar stationed at the DOE-ARM measurement site in Lamont, Oklahoma during MC3E, (b) GridRad data created at equivalent time resolution, and (c) vertically pointing S-band radar data smoothed in altitude and time at scales consistent with the GridRad procedure. These observations were taken from 00:00 to 17:30 UTC on 20 May 2011. The GridRad echo boundary is superimposed in (a) to enable direct comparison (gray line).

with the melting level (the so-called “bright band”) well-defined in stratiform rain regions in the MC3E data and less defined in the GridRad data (e.g., between altitudes of 3 and 4 km prior to 550 min and after 650 min). The magnitude of Z_H is also commonly ~ 5 dBZ lower in GridRad data, though such differences are largely reduced if the MC3E data is smoothed to emulate the GridRad binning procedure. Furthermore, remaining differences following smoothing of the MC3E data would likely be reduced further if the intrinsic horizontal smoothing of GridRad data could be reproduced (this is impossible because the MC3E data is a point measurement). Second, though differences in Z_H are apparent, the echo boundaries (i.e., echo top and bottom) are largely consistent between the two datasets. The contributing depth restriction imposed during Step 2 of the GridRad procedure is largely responsible for such agreement.

The second dataset comparison provided here demonstrates the potential for multi-sensor analyses using GridRad data and similar datasets from space-based sensors obtained at higher space and time resolution. In particular, Figure 6 shows vertical profiles taken by the Cloud-Aerosol Lidar with Orthogonal Polarization (CALIOP) aboard the CALIPSO satellite (Winker et al., 2009) and the Cloud Profiling Radar (CPR) aboard the CloudSat satellite (Stephens et al., 2002), both of which operate in close succession within the shared orbit of the NASA Afternoon constellation of satellites (or A-Train). The GridRad data shown in this example were created at the satellite overpass times. The differences in the spatial resolution of these datasets is clear, given that the CALIOP data is obtained at a spatial resolution of $335\text{--}1000\text{ m} \times 30\text{--}60\text{ m}$ ($\Delta x \times \Delta z$) and the CPR data is obtained at a spatial resolution of $1.1\text{ km} \times 240\text{ m}$ ($\Delta x \times \Delta z$). The combined sampling of all three systems, however, demonstrates that the GridRad data: i) provide Z_H echo top altitudes that are consistent with the CloudSat CPR (see also Fig. 7), and ii) help to fill in the depth of the cloud that is not well sampled by CALIOP and CPR, given that both satellite-based sensors suffer from attenuation in volumes with large precipitation-sized particles.

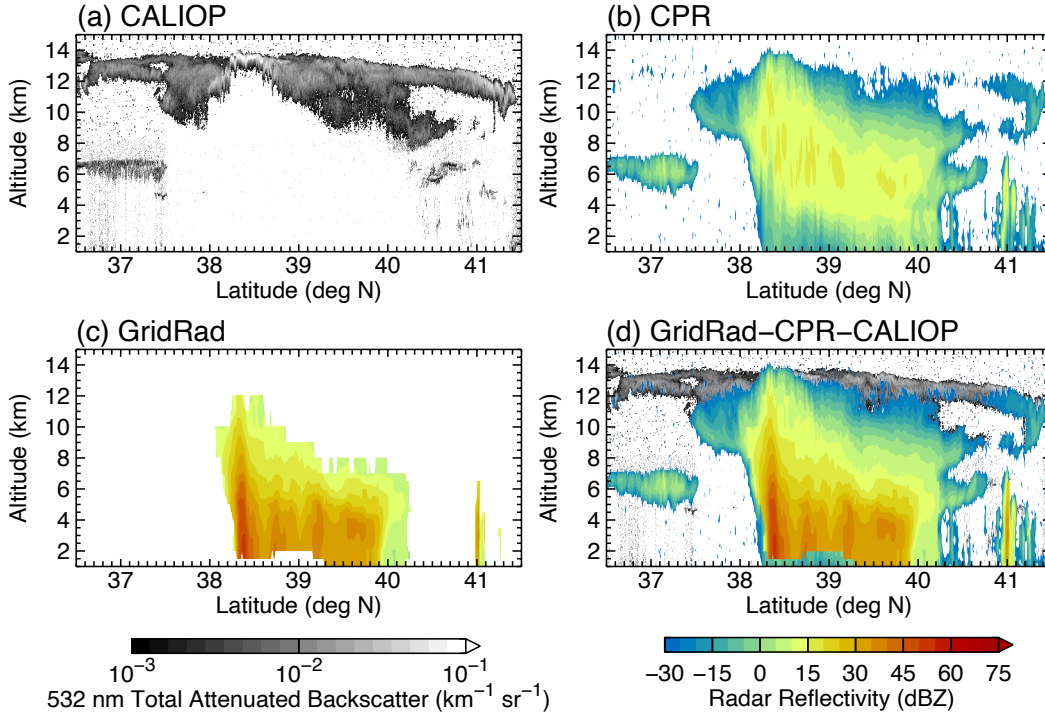


Figure 6: For a CONUS overpass by the A-Train on 8 June 2015 from 0808 to 0810 UTC: (a) CALIOP 532 nm total attenuated backscatter, (b) CloudSat CPR radar reflectivity, (c) GridRad radar reflectivity Z_H , and (d) an overlay of all three datasets.

4.2 Limitations

In addition to the limitations of spatial resolution and frequency of the available GridRad data, one of the most important limitations users should consider is the minimum detectable Z_H . NEXRAD WSR-88D radars are capable of sensing Z_H well below the scale of dense precipitable hydrometeors, especially at close ranges from the radar. The minimum detectable signal of the radar is -42 dBZ at 1 km and increases with increasing range to about 11 dBZ at the maximum detectable range of 460 km (Crum and Alberty, 1993). For the observations merged in the GridRad procedure (i.e., those within 300 km of each radar), the

minimum detectable $Z_H \leq 7.5$ dBZ. Thus, data merged into the GridRad domain can span a wide range of Z_H , especially considering that the maximum observed Z_H in storms over the CONUS is about 80 dBZ. Nevertheless, the vast majority of Z_H in GridRad is ≥ 5 dBZ.

Apart from the obvious limitations related to resolution, sampling, Level 2 data availability, and the temporal availability of the public GridRad datasets outlined above, there are sources of error in the native NEXRAD WSR-88D Level 2 observations that propagate into the GridRad data (i.e., artifacts that are not removed during the 4-step GridRad procedure) which users should expect to encounter. Short descriptions of such error are provided below, with discussion limited to the most common errors. Many of these errors can be largely mitigated through use of the available quality control routines discussed in §5 below.

One of the most common sources of error in radar observations is non-standard beam refraction (commonly referred to as ‘anomalous propagation’ or AP). As outlined in §3 above, the altitude of each beam in a radar volume used for binning in the GridRad procedure is calculated assuming a standard index of refraction for the atmosphere. Under dry, near-adiabatic conditions in the lower atmosphere, radar beams can refract less than expected and result in an underestimation of the true beam altitude for binning. Conversely, over-estimation of the radar beam altitude is possible if the beam refracts more than expected, which is common if there are significant temperature inversions in the tropospheric boundary layer. These errors from non-standard refraction, however, are typically limited to beams that travel long distances in the boundary layer (e.g., [Doviak and Zrnić, 1993](#)). A correction for this source of error does not exist in the provided GridRad quality control routines.

Contamination of the radar measurement from beam side lobes is also a common source of error in radar observations, but is relatively rare at Z_H observed within the GridRad data. In general, side lobe contamination is only possible from the first lobe, which is 27 dBZ below the main lobe power for a NEXRAD WSR-88D radar and 1.2 degrees away from the beam center (up to 6 km in altitude for ranges within 300 km). In order for side lobe contamination to be present, the Z_H of the scatterer in the path of the side lobe must be stronger than the signal in the path of the main lobe by at least the two-way, first-side lobe isolation (i.e., ≥ 54 dBZ, [OFCM, 2005](#)). At the typical 5 dBZ minimum of Z_H in GridRad data, side lobe contamination of a given beam requires that Z_H within 1.2 degrees of the beam center exceed 59 dBZ. A correction for this source of error is possible using the provided GridRad quality control routines.

The sun emits radiation at all wavelengths. During sunrise and sunset, NEXRAD WSR-88D radars may receive such radiation within beams coincident with the sun’s inclination, leading to Z_H typically less than 20 dBZ that is confined to a few azimuthal samples at a single elevation. Such radar signals are commonly referred to as ‘sun strobes’ and are observed when clouds are not present along the line of sight to the sun. This error is almost entirely mitigated using the provided GridRad quality control routines. Note that sun strobes are somewhat analogous to interference detected from microwave transmitters near the WSR-88D radars, which can be a more persistent source of error, but is also well-mitigated using the provided GridRad quality control routines.

Some common error sources only impact the polarimetric variables Z_{DR} , ϕ_{DP} , and ρ_{HV} . In many cases, these errors can be uniquely informative of the observed storm’s microphysics and often occur downrange of convection. Such error sources include differential attenuation, depolarization, and non-uniform beam filling (NBF). Examples of these and less common error sources can be found in [Kumjian \(2013\)](#). Unless ρ_{HV} is reduced well below 1.0, many of these error sources are not removed using the available quality control routines. Differential attenuation of the H and V beams is only common in broad areas of heavy precipitation in NEXRAD WSR-88D observations (e.g., [Ryzhkov et al., 2013](#); [Kumjian, 2013](#)). In the event

that differential attenuation does occur, it is manifested as negatively biased Z_{DR} downrange of the attenuating scatterers (often the responsible medium is large hail).

Depolarization can cause radially oriented streaks of positive or negative Z_{DR} when ice crystals are oriented at a nonzero angle relative to the H and V polarization plane axes (e.g., [Ryzhkov and Zrnić, 2007](#)). These depolarization streaks are most evident downrange of the depolarizing medium and are common in anvil regions of deep convection and in some wintertime storms.

NBF can cause negative Z_{DR} biases for very large cross-beam gradients of measured Z_H and Z_{DR} at distant ranges, but only if the cross-beam gradients are of opposite sign ([Ryzhkov, 2007](#)). These biases begin at the region of NBF and extend downrange. If both Z_H and Z_{DR} are decreasing with increasing elevation, the NBF-induced Z_{DR} bias would be positive. If there is no existing Z_{DR} gradient in the first place, there would be no NBF-induced bias in Z_{DR} . While the space-time weighting in the GridRad procedure helps to limit NBF in the output volumes, such errors may be present from time to time in the GridRad data.

5 Example Code and GridRad Data Usage

To enable easy access and use of the v4.2 GridRad data, we have provided sample read and quality control routines written in the *IDL* (*Interactive Data Language*) and *Python* programming languages. Table 2 lists these routines and their utility.

Procedure Name (language)	Input	Purpose
<code>gridrad.read_file</code> (IDL) <code>gridrad.read_file</code> (Python)	Full path to location of GridRad file.	Read contents of GridRad file.
<code>gridrad.filter</code> (IDL) <code>gridrad.filter</code> (Python)	GridRad data structure from <code>gridrad.read_file</code> .	Remove observations with low echo frequency or W .
<code>gridrad.remove_clutter</code> (IDL) <code>gridrad.remove_clutter</code> (Python)	GridRad data structure from <code>gridrad.read_file</code> .	Remove echo that is objectively flagged as non-meteorological.

Table 2: Name, input, and purpose of provided code to read and quality control the GridRad data. The IDL code is provided as three separate procedures with file names that match the procedure names (with a ‘.pro’ file extension). The Python programs are provided as a single file (‘gridrad.py’).

To reduce file size, the GridRad data files use a combination of a sparse storage scheme and internal netCDF-4 file compression. Data values for V and W are stored in one-dimensional arrays only for those GridRad grid volumes that contain echo. A one-dimensional zero-based index array of the same size is provided to scatter the data values into the full three-dimensional GridRad arrays. The index array assumes that the longitude subscript of the GridRad array varies fastest, followed by the latitude subscript, and then the altitude subscript. The echo count (N_{echo}) and observation count (N_{obs}) are stored as full three-dimensional arrays. The provided *IDL* and *Python* file reading programs return the full, three-dimensional arrays of GridRad data to the user and can be used as additional reference for the above-outlined procedure. Filtering and decluttering methods are discussed in the following section.

5.1 Recommendations

The GridRad data provided in the public archives contain the raw outputs of the 4-step GridRad procedure. The data are built using every available successful NEXRAD WSR-88D Level 2 observation, including those with possible artifacts or non-meteorological scatter. Thus, for users who aim to study and/or evaluate high-quality meteorological echo, it is recommended that two quality control techniques be applied to the data prior to analysis. First, many low-quality observations and scanning artifacts can be removed by evaluating the frequency at which echo is present within all available NEXRAD observations (referred to here as ‘filtering’). This is the central idea behind the `gridrad.filter` programs, which identify GridRad volumes with low W (< 1.5) or low echo frequency ($N_{\text{echo}}/N_{\text{obs}} < 0.6$, if $N_{\text{obs}} \geq 3$) and removes the binned radar variables (sets them equal to a not-a-number). The goal of this filtering approach is to retain echo that has either been observed consistently from multiple Level 2 scans or was made in close proximity to a contributing radar and close in time to that of the GridRad analysis. To demonstrate the benefit of filtering, we provide an example analysis comparing $Z_H = 5$ dBZ echo top altitudes computed using GridRad data and higher-resolution CloudSat CPR data in Figure 7. No attempt was made to account for differences resulting from the mismatched W- and S-band frequencies of the CPR and NEXRAD radars in this analysis, but that difference is expected to be small at a reflectivity threshold of 5 dBZ. This comparison shows that 5-dBZ echo top altitudes based on the raw GridRad data are biased nearly 1 km high, those based on the recommended $N_{\text{echo}}/N_{\text{obs}}$ filtering threshold of 0.6 are nearly unbiased, and those based on the highest

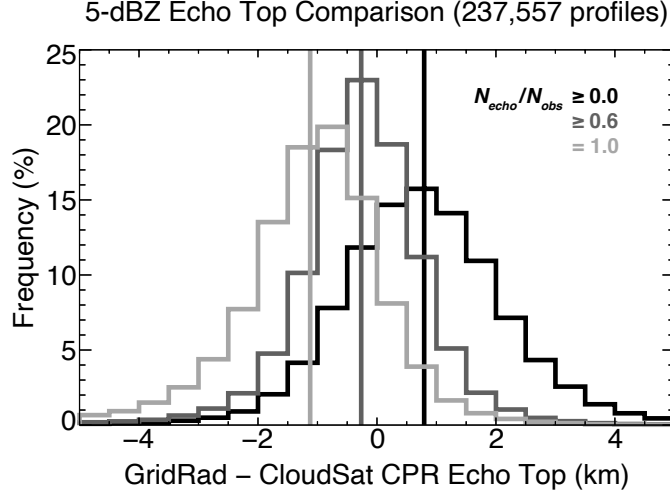


Figure 7: Frequency distributions of $Z_H = 5$ dBZ echo top altitude differences between those diagnosed using GridRad data and those from higher-resolution CloudSat Cloud Profiling Radar (CPR) observations. Distributions are shown for echo frequency thresholds N_{echo}/N_{obs} of 0.0 (black), 0.6 (dark gray), and 1.0 (light gray). This comparison is based on 237,557 observed Z_H profiles between 2006 and 2016.

possible threshold of 1.0 (or 100%) are biased nearly 1 km low. Thus, we recommend that GridRad data used for meteorological studies be filtered.

The `gridrad_remove_clutter` programs are designed to remove non-meteorological echo from biological scatterers and artifacts such as noisy returns or ‘speckles.’ The approaches employed are largely modeled after the ideas outlined in Zhang et al. (2004) for native NEXRAD WSR-88D Level 2 volumes. First, GridRad volumes containing echo are checked for additional echo in immediately adjacent volumes at the same altitude. If the total echo coverage in the neighboring grid volumes (and the volume in question) is less than 32%, the reflectivity is changed to a missing value. Second, GridRad columns with weak echo that is contained entirely within the lowest altitude levels are removed. This second step will remove some meteorological echo in shallow precipitation (mostly winter storms) and thus is optional in the `gridrad_remove_clutter` routine. Third, non-meteorological echo below the anvils of deep convection is removed. This step requires a layer of echo-free GridRad volumes between the anvil in the upper troposphere and (mostly biological) scatter in the tropospheric boundary layer. Last, a second check for sufficient echo coverage is applied that is equivalent to the first step. It is recommended that the full 4-step clutter removal process be used for analysis of deep cloud systems and that shallow echo removal (the optional Step 2) not be used for shallow cloud systems.

For GridRad volumes that contain the polarimetric variables, a ρ_{HV} -based step of clutter removal is added before the general 4-step procedure outlined above. Namely, echoes are discarded if $Z_H < 40$ dBZ and $\rho_{HV} < 0.9$ or, if at altitudes at or above 10 km AMSL, $Z_H < 25$ dBZ and $\rho_{HV} < 0.95$. This approach leverages one of the key strengths of ρ_{HV} observations: distinguishing between meteorological and non-meteorological echo.

Figure 8 shows column-maximum Z_H from an example polarimetric GridRad analysis with all possible combinations of quality control applied. This analysis time has convection over the Great Plains and Rocky Mountains and multiple precipitation regimes along the east coast of the United States. In the raw data, biological scatterers are present over the entire U.S., evidenced by circular low- Z_H (< 15 dBZ) features at

GridRad Column-Maximum Maps valid 2018-07-28 00:00 UTC

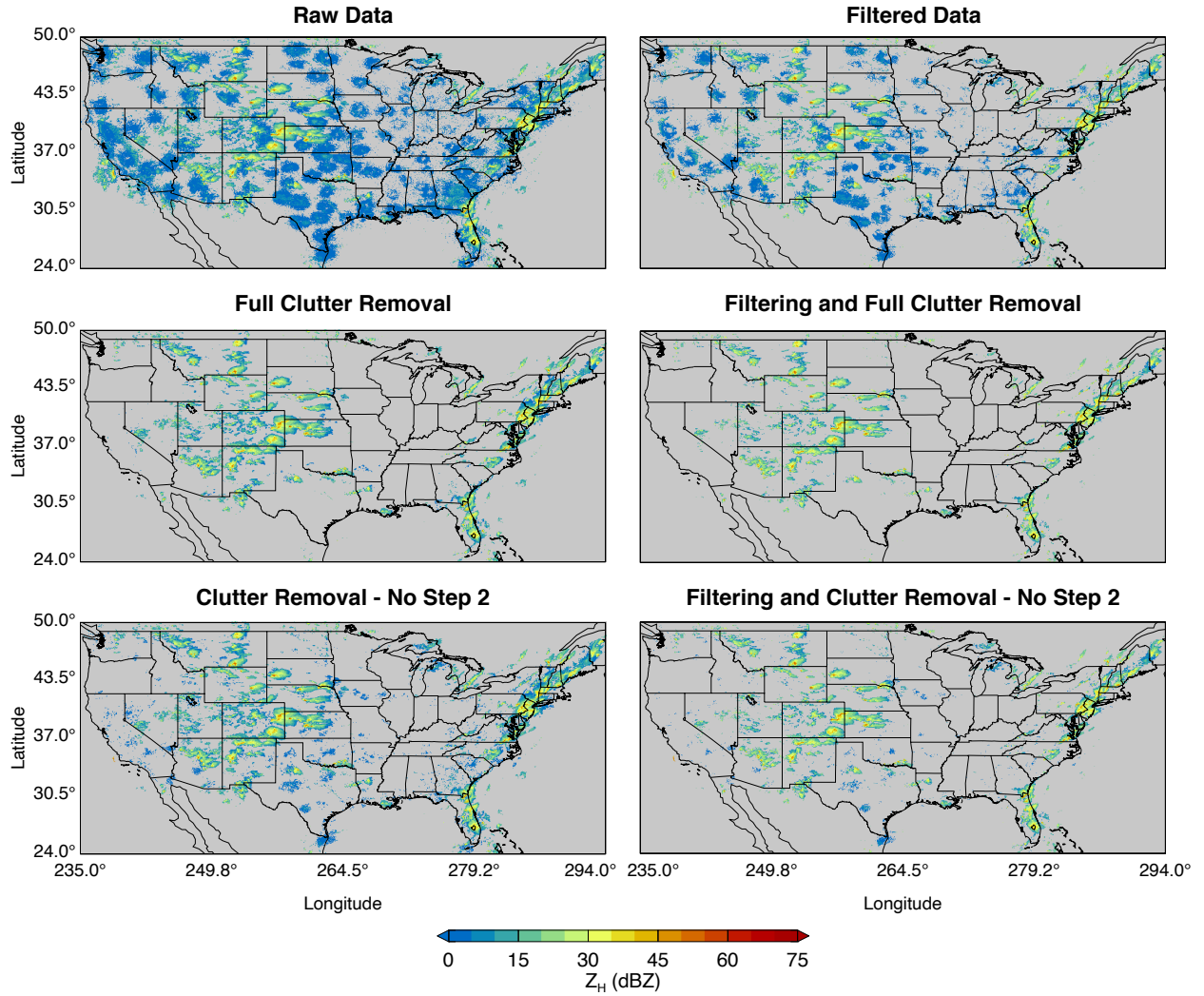


Figure 8: Maps of GridRad column-maximum Z_H with and without all possible combinations of the provided quality control techniques. The GridRad analysis is valid 28 July 2018 at 00:00 UTC.

near ranges to the contributing radar locations. These non-meteorological echoes are effectively removed through application of one or more of the possible combinations of quality control techniques.

5.2 GridRad Examples of Common Radar Analyses

The GridRad data enable novel analyses of observed clouds and precipitation over the CONUS. Past uses of GridRad data include evaluating and testing convective parameterizations in global climate models (e.g., Jeyaratnam et al., 2020; Wang et al., 2021), training machine learning models to predict storm-related hazards (e.g., Lagerquist et al., 2020; Mecikalski et al., 2021), evaluating resolved convection simulated by non-hydrostatic models (e.g., Thielen and Gallus Jr., 2019; Zhang et al., 2019; Coleman and Ancell, 2020; Lin et al., 2021; Phoenix and Homeyer, 2021), validating satellite methods that are used in regions without a dense radar network (e.g., Apke et al., 2018; Wang et al., 2019; Cooney et al., 2021), and event-based and/or

climatological studies of precipitating systems in the extratropics to advance our understanding of a range of meteorological, climatological, and hydrological processes (e.g., [Cooney et al., 2018](#); [Feng et al., 2019](#); [Murillo and Homeyer, 2019](#); [Sandmæl et al., 2019](#); [Starzec et al., 2020](#); [Homeyer et al., 2020](#); [Jeong et al., 2020](#); [Schumacher and Rasmussen, 2020](#); [Homeyer et al., 2021](#); [Homeyer and Bowman, 2021](#); [Murillo et al., 2021](#); [Tinney and Homeyer, 2021](#)). To provide users with some insight into these possibilities, an example interrogation of an event using GridRad-Severe data is presented here. All of the example figures were produced using the *GridRad Viewer* software developed by C. Homeyer in *IDL* and made available online at [GridRad.org](#). The full recommendations for quality control were applied to the GridRad data used in these examples.

Figure 9 shows maps of column-maximum Z_H at 4-hour intervals from the GridRad-Severe data for the 20 May 2013 event, widely known due to the catastrophic EF-5 tornado that passed through the town of Moore, Oklahoma between 19:56 and 20:33 UTC. Maps encompassing the entire event domain are given from the time of the severe supercell storms in Oklahoma during the Moore tornado (20 UTC; Fig. 9a) through the overnight hours as the storms in Oklahoma and nearby states increased and grew upscale into a large, multi-state mesoscale convective system that began to dissipate the following morning (00-08 UTC on 21 May 2013; Figs. 9b-d).

Figure 10 shows Z_H and derived products for a subdomain of the 20:00 UTC analysis on 20 May 2013 focused on at least three supercell storms in far North Texas and central Oklahoma. Figures 10a and 10b show column-maximum Z_H and Z_H at a constant altitude of 2 km AMSL, respectively, revealing areas of precipitation and related echo aloft (non-precipitating cloud, most being anvil produced by deep convection). The three supercell storms are highlighted further by the attempts to estimate maximum potential hail size and dominant hydrometeor type in Figures 10c and 10d. Namely, Figure 10c shows the Z_H -based Maximum Expected Size of Hail fit to the 95th percentile diameter of hail reports (MESH₉₅), recently defined in [Murillo and Homeyer \(2019\)](#). MESH₉₅ (and related variants) is based on the vertical integral of Z_H above the height of the 0°C isotherm (set to a constant altitude of 4 km AMSL in this case, based on nearby balloon observations) and, for otherwise supportive dynamic and thermodynamic environments, is skillful in capturing the maximum hail produced by a severe storm (e.g., [Murillo and Homeyer, 2019](#); [Murillo et al., 2021](#); [Wendt and Jirak, 2021](#)). The three supercells highlighted in this map were responsible for multiple severe hail reports ranging from 1 to 2.5 in. (25-65 mm) in diameter, consistent with the magnitudes estimated by MESH₉₅. The polarimetric hydrometeor classification in Figure 10d (at an altitude of 2 km AMSL) is based on the operational NEXRAD WSR-88D algorithm ([Park et al., 2009](#)), slightly revised and applied as outlined in [Handler and Homeyer \(2018\)](#). The hydrometeor classification algorithm uses Z_H , Z_{DR} , K_{DP} , and ρ_{HV} to determine the most likely hydrometeor type. Convection-stratiform echo classifications and the height of the 0°C isotherm are also used in the algorithm, for which echo classifications are determined by the Storm Labeling in 3 Dimensions algorithm (SL3D; [Starzec et al., 2017](#)), which was developed using GridRad data. The three supercells show broad areas classified as heavy rain at 2 km AMSL, with the Moore, Oklahoma tornadic supercell storm (that bisected by the A–B line in Fig. 10a) showing areas of large ice (graupel and hail) as well, indicating the most likely location of hail reaching the ground at this time. Such analysis techniques (i.e., the hydrometeor classification) demonstrate the unique information given by polarimetric observations to improve hazard identification in severe storms.

While the spatial information provided by maps is useful to assessing the overall impact of an event, many studies of radar observations investigate the vertical structure of storms to better understand the complex processes leading to hazards at the ground and to what altitudes storm impacts on atmospheric composition and aviation (i.e., turbulence) are possible. Figure 11 shows vertical cross-sections of Z_H , azimuthal shear, Z_{DR} , K_{DP} , ρ_{HV} , and the hydrometeor classification taken along the path labeled ‘A–B’ in Fig. 10a

Column-Maximum Maps for 2013-05-20 GridRad-Severe Event

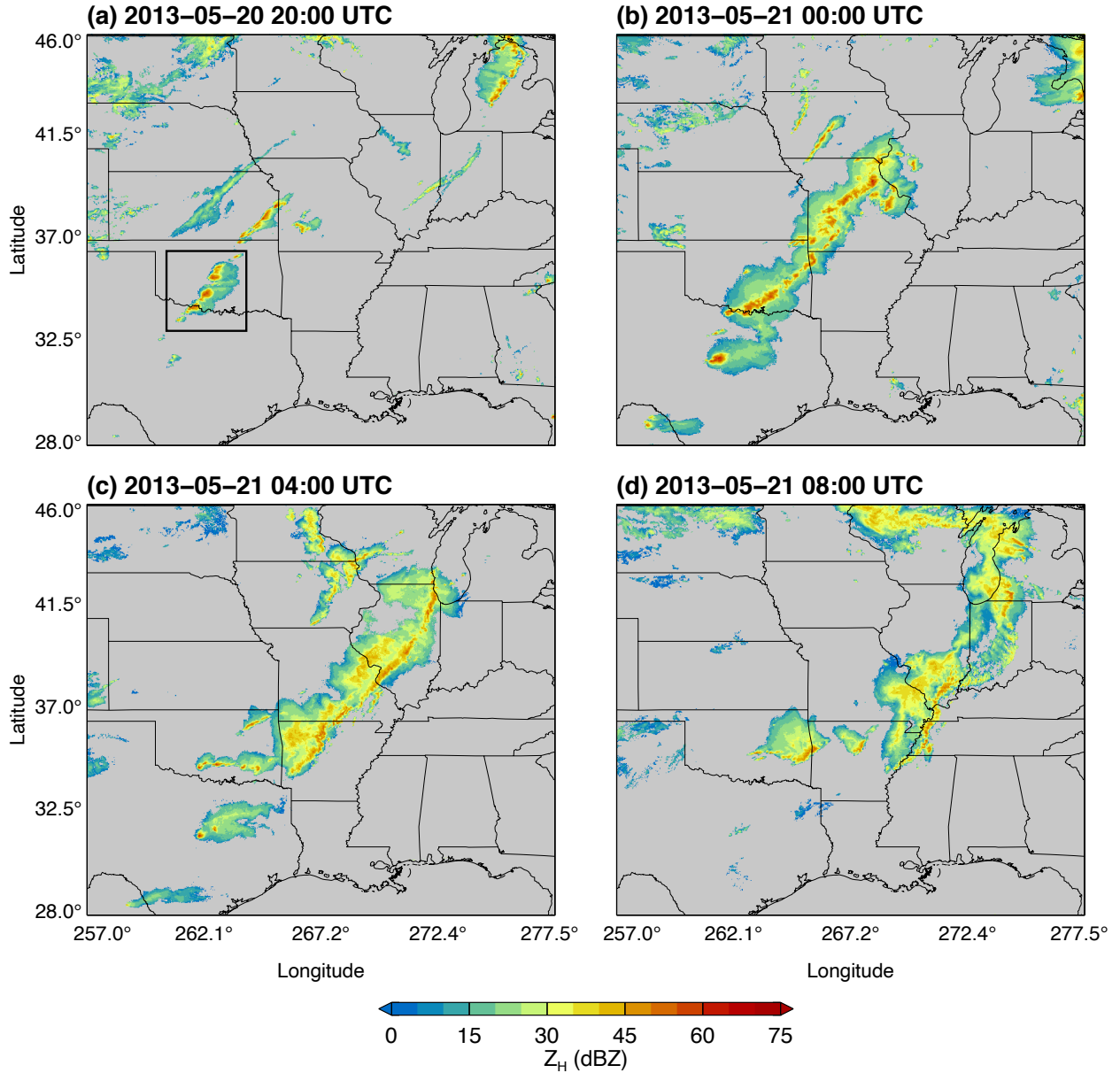


Figure 9: For the GridRad Severe 20 May 2013 event: maps of column-maximum Z_H valid (a) 20 UTC on 20 May 2013, (b) 00 UTC on 21 May 2013, (c) 04 UTC on 21 May 2013, and (d) 08 UTC on 21 May 2013. The thick black box in (a) encompasses the smaller analysis domain used in Fig. 10.

and bisecting the Moore, Oklahoma tornadic supercell storm. Several features common to deep convection and supercell storms can be identified in these cross-sections, including updraft signatures such as the bounded weak echo region in Z_H (BWER; e.g., [Browning and Donaldson Jr., 1963](#); [Musil et al., 1986](#); [Calhoun et al., 2013](#)) and columns of large positive values in Z_{DR} and K_{DP} (e.g., [Kumjian et al., 2014](#); [Homeyer and Kumjian, 2015](#)) on the left of the cross-section, the vertical structure of the tornadic mesocyclone (cyclonically rotating updraft) in azimuthal shear (also on the left of the cross-section), and the graupel and hail dominance within the supercell given by the combined analysis of the polarimetric variables via

Maps for 2013-05-20 GridRad-Severe Event valid 20:00 UTC

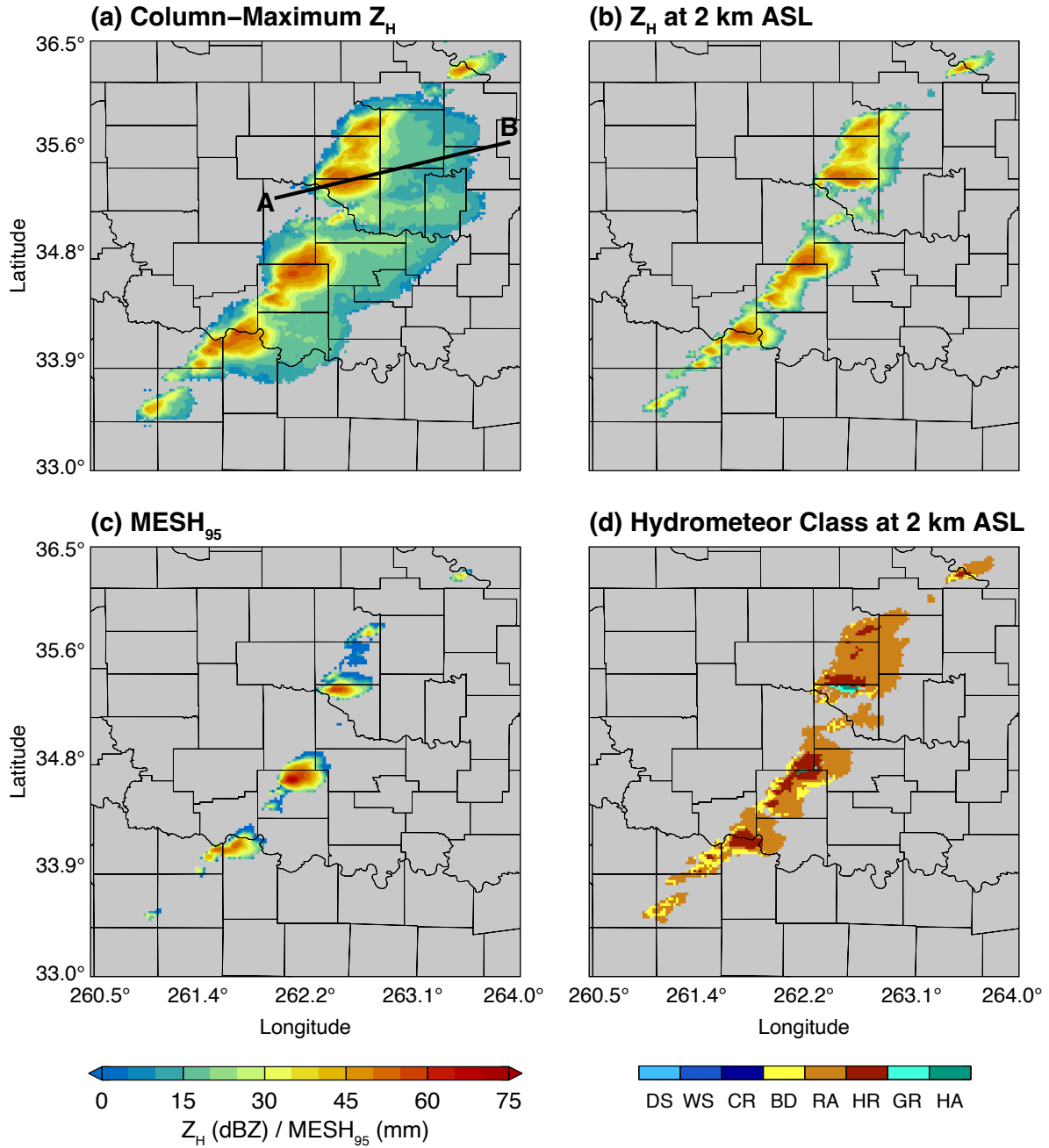


Figure 10: For the 20 May 2013 at 20 UTC GridRad-Severe analysis, maps of (a) column-maximum Z_H , (b) Z_H at an altitude of 2 km, (c) $MESH_{95}$, and (d) polarimetric hydrometeor classification. For (d), the hydrometeor classes are: dry aggregated snow (DS), wet snow (WS), ice crystals of various orientations (CR), “big drops” (BD), light and moderate rain (RA), heavy rain (HR), graupel (GR), and hail (HA). The thick black line labeled ‘A–B’ in (a) represents the path of the vertical cross-sections provided in Fig. 11.

the hydrometeor classification. Reduced coverage of the kinematic fields, which is common relative to the microphysical quantities in GridRad data, is evidenced by the large data void in the azimuthal shear cross-

section here. Though this example provides only a single snapshot of vertical structure, the GridRad data allow for extensive 3-D analysis of storms, as demonstrated in several prior studies cited herein.

Vertical Sections for 2013-05-20 GridRad-Severe Event valid 20:00 UTC

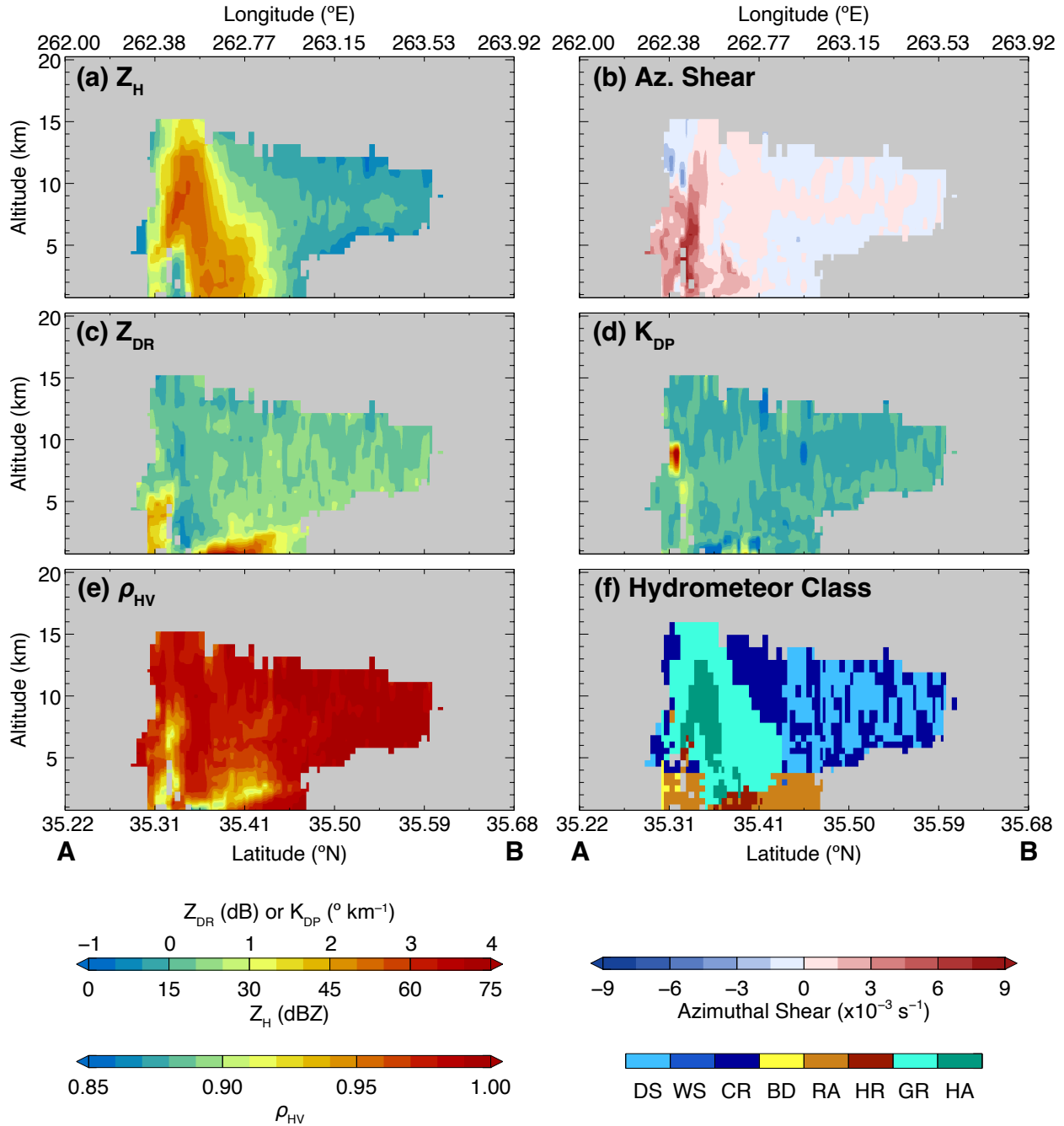


Figure 11: Vertical cross-sections of (a) Z_H , (b) Z_{DR} , (c) K_{DP} , (d) ρ_{HV} , and (e) polarimetric hydrometeor classification along the line labeled 'A-B' in Fig. 10a. Hydrometeor classes in (d) are as those shown in Fig. 10.

6 Table of Symbols

Symbol	Units and/or numerical value	Quantity
Z_H	dBZ	radar reflectivity at horizontal polarization
V_R	m s^{-1}	radial velocity from Doppler shift
σ_V	m s^{-1}	velocity spectrum width
Z_{DR}	dB	differential radar reflectivity
ϕ_{DP}	$^{\circ}$	differential propagation phase shift
K_{DP}	$^{\circ} \text{ km}^{-1}$	specific differential phase
ρ_{HV}	dimensionless	co-polar correlation coefficient
L	150 km	spatial weighting scale
τ	150 s	temporal weighting scale
r	km	radial distance from the radar
Δt	s	time difference between observation and analysis
x, x_i	$^{\circ}\text{E}$	longitude
y, y_j	$^{\circ}\text{N}$	latitude
z, z_k	km	altitude with respect to the geoid
w_i	dimensionless	weight for a single radar observation
W	dimensionless	total weight
v_i		single observation of a radar variable
V		weighted average of a radar variable
N_{obs}	dimensionless	number of observations in GridRad volume
N_{echo}	dimensionless	number of observations with echo in GridRad volume
Δx	km	horizontal resolution
Δz	km	altitude resolution
Δr	km	radial resolution of Level 2 observation
ℓ	km	radar beam width or depth

7 References Cited

- Apke, J. M., J. R. Mecikalski, K. Bedka, E. W. McCaul, C. R. Homeyer, and C. P. Jewett, 2018: Relationships between deep convection updraft characteristics and satellite-based super rapid scan mesoscale atmospheric motion vector-derived flow. *Mon. Wea. Rev.*, **146**, 3461–3480, doi:10.1175/MWR-D-18-0119.1.
- Borowska, L., D. Zrnić, A. Ryzhkov, P. Zhang, and C. Simmer, 2011: Polarimetric estimates of a 1-month accumulation of light rain with a 3-cm wavelength radar. *J. Hydrometeor.*, **12**, 1024–1039, doi:10.1175/2011JHM1339.1.
- Browning, K. A., and R. J. Donaldson Jr., 1963: Airflow and structure of a tornadic storm. *J. Atmos. Sci.*, **20**, 533–545.
- Calhoun, K. M., D. R. MacGorman, C. L. Ziegler, and M. I. Biggerstaff, 2013: Evolution of lightning activity and storm charge relative to dual-doppler analysis of a high-precipitation supercell storm. *Mon. Wea. Rev.*, **141**, 2199–2223, doi:10.1175/MWR-D-12-00258.1.
- Coleman, A., and B. Ancell, 2020: Toward the improvement of high-impact probabilistic forecasts with a sensitivity-based convective-scale ensemble subsetting technique. *Mon. Wea. Rev.*, **148**, 4995–5014, doi:10.1175/MWR-D-20-0043.1.
- Cooney, J. W., K. M. Bedka, K. P. Bowman, K. V. Khlopenkov, and K. Itterly, 2021: Comparing tropopause-penetrating convection identifications derived from NEXRAD and GOES over the contiguous united states. *J. Geophys. Res. Atmos.*, **126**, e2020JD034 319, doi:10.1029/2020JD034319.
- Cooney, J. W., K. P. Bowman, C. R. Homeyer, and T. M. Fenske, 2018: Ten-year analysis of tropopause-overshooting convection using gridrad data. *J. Geophys. Res. Atmos.*, **123**, 329–343, doi:10.1002/2017JD027718.
- Crum, T. D., and R. L. Alberty, 1993: The WSR-88D and the WSR-88D operational support facility. *Bull. Amer. Meteorol. Soc.*, **74** (9), 1669–1687.
- Cunningham, J. G., W. D. Zittel, R. R. Lee, and R. L. Ice, 2013: Methods for identifying systematic differential reflectivity (Z_{DR}) biases on the operational WSR-88D network. *36th Conf. on Radar Meteorology*, Amer. Meteor. Soc., 9B.5.
- Doviak, R. J., and D. S. Zrnić, 1993: *Doppler Radar and Weather Observations*. 2nd ed., ISBN 0-486-45060-0, Dover Publications, Inc., 31 East 2nd Street, Mineola, NY, 11501.
- Feng, Z., R. A. Houze, L. R. Leung, F. Song, J. C. Hardin, J. Wang, W. I. Gustafson, and C. R. Homeyer, 2019: Spatiotemporal characteristics and large-scale environments of mesoscale convective systems east of the Rocky Mountains. *J. Clim.*, **32**, 7303–7328, doi:10.1175/JCLI-D-19-0137.1.
- Handler, S. L., and C. R. Homeyer, 2018: Radar-observed bulk microphysics of midlatitude leading line trailing stratiform mesoscale convective systems. *J. Appl. Meteor. Climatol.*, **57**, 2231–2248, doi:10.1175/JAMC-D-18-0030.1.
- Helmus, J. J., and S. M. Collis, 2016: The Python ARM Radar toolkit (Py-ART), a library for working with weather radar data in the Python programming language. *J. Open Research Software*, **4**(1), p.e25, doi:10.5334/jors.119.

- Homeyer, C. R., 2014: Formation of the enhanced-v infrared cloud top feature from high-resolution three-dimensional radar observations. *J. Atmos. Sci.*, **71**, 332–348, doi:10.1175/JAS-D-13-079.1.
- Homeyer, C. R., and K. P. Bowman, 2021: A 22-year evaluation of convection reaching the stratosphere over the united states. *J. Geophys. Res. Atmos.*, **126**, doi:10.1029/2021JD034808.
- Homeyer, C. R., and M. R. Kumjian, 2015: Microphysical characteristics of overshooting convection from polarimetric radar observations. *J. Atmos. Sci.*, **72**, 870–891, doi:10.1175/JAS-D-13-0388.1.
- Homeyer, C. R., T. N. Sandmæl, C. K. Potvin, and A. M. Murphy, 2020: Distinguishing characteristics of tornadic and nontornadic supercell storms from composite mean analyses of radar observations. *Mon. Wea. Rev.*, **148**, 5015–5040, doi:10.1175/MWR-D-20-0136.1.
- Homeyer, C. R., and Coauthors, 2021: Polarimetric signatures in landfalling tropical cyclones. *Mon. Wea. Rev.*, **149**, 131–154, doi:10.1175/MWR-D-20-0111.1.
- Jensen, M. P., and Coauthors, 2016: The Midlatitude Continental Convective Clouds Experiment (MC3E). *Bull. Amer. Meteorol. Soc.*, **97**, 1667–1686, doi:10.1175/BAMS-D-14-00228.1.
- Jeong, J.-H., J. Fan, C. R. Homeyer, and Z. Hou, 2020: Understanding hailstone temporal variability and contributing factors over the U.S. Southern Great Plains. *J. Clim.*, **33**, 3947–3966, doi:10.1175/JCLI-D-19-0606.1.
- Jeyaratnam, J., J. F. Booth, C. M. Naud, Z. J. Luo, and C. R. Homeyer, 2020: Upright convection in extratropical cyclones: A survey using ground-based radar data over the united states. *Geophys. Res. Lett.*, **47**, e2019GL086620, doi:10.1029/2019GL086620.
- Kumjian, M. R., 2013: Principles and applications of dual-polarization weather radar. Part III: Artifacts. *J. Operational Meteor.*, **1** (21), 265–274.
- Kumjian, M. R., A. P. Khain, N. Benmoshe, E. Ilotoviz, A. V. Ryzhkov, and V. T. J. Phillips, 2014: The anatomy and physics of Z_{DR} columns: Investigating a polarimetric radar signature with a spectral bin microphysical model. *J. Appl. Meteor. Climatol.*, **53**, 1820–1843, doi:10.1175/JAMC-D-13-0354.1.
- Lagerquist, R., A. McGovern, C. R. Homeyer, D. J. Gagne II, and T. Smith, 2020: Deep learning on three-dimensional multiscale data for next-hour tornado prediction. *Mon. Wea. Rev.*, **148**, 2837–2861, doi:10.1175/MWR-D-19-0372.1.
- Langston, C., J. Zhang, and K. Howard, 2007: Four-dimensional dynamic radar mosaic. *J. Atmos. Oceanic Technol.*, **24**, 776–790, doi:10.1175/JTECH2001.1.
- Lin, Y., J. Fan, J.-H. Jeong, Y. Zhang, C. R. Homeyer, and J. Wang, 2021: Urbanization-induced land and aerosol impacts on storm propagation and hail characteristics. *J. Atmos. Sci.*, **78**, 925–947, doi:10.1175/JAS-D-20-0106.1.
- Mecikalski, J. R., T. N. Sandmæl, E. M. Murillo, C. R. Homeyer, K. M. Bedka, J. M. Apke, and C. P. Jewett, 2021: A random-forest model to assess predictor importance and nowcast severe storms using high-resolution radar–GOES satellite–lightning observations. *Mon. Wea. Rev.*, **149**, 1725–1746, doi:10.1175/MWR-D-19-0274.1.
- Melnikov, V. M., R. J. Doviak, D. S. Zrnić, and D. J. Stensrud, 2011: Mapping Bragg scatter with a polarimetric WSR-88D. *J. Atmos. Oceanic Technol.*, **28**, 1273–1285, doi:10.1175/JTECH-D-10-05048.1.

- Melnikov, V. M., R. J. Doviak, D. S. Zrnić, and D. J. Stensrud, 2013: Structures of Bragg scatter observed with the polarimetric WSR-88D. *J. Atmos. Oceanic Technol.*, **30**, 1253–1258, doi:10.1175/JTECH-D-12-00210.1.
- Melnikov, V. M., D. S. Zrnić, R. J. Doviak, and J. K. Carter, 2003: Calibration and performance analysis of NSSL’s polarimetric WSR-88D. *NOAA/NSSL Report*, 77 pp.
- Murillo, E. M., and C. R. Homeyer, 2019: Severe hail fall and hailstorm detection using remote sensing observations. *J. Appl. Meteor. Climatol.*, **58**, 947–970, doi:10.1175/JAMC-D-18-0247.1.
- Murillo, E. M., C. R. Homeyer, and J. T. Allen, 2021: A 23-year severe hail climatology using GridRad MESH observations. *Mon. Wea. Rev.*, **149**, 945–958, doi:10.1175/MWR-D-20-0178.1.
- Musil, D. J., A. J. Heymsfield, and P. L. Smith, 1986: Microphysical characteristics of a well-developed weak echo region in a high plains supercell thunderstorm. *J. Climate Appl. Meteor.*, **25**, 1037–1051.
- OFCM, 2005: Federal Meteorological Handbook No. 11 – Doppler Radar Meteorological Observations, Part B: Doppler Radar Theory and Meteorology. FCM-H11B-2005 (Available online at <http://www.ofcm.gov/publications/fmh/allfmh2.htm>).
- OFCM, 2006: Federal Meteorological Handbook No. 11 – Doppler Radar Meteorological Observations, Part C: WSR-88D Products and Algorithms. FCM-H11C-2006 (Available online at <http://www.ofcm.gov/publications/fmh/allfmh2.htm>).
- Park, H., A. V. Ryzhkov, D. S. Zrnić, and K.-E. Kim, 2009: The hydrometeor classification algorithm for the polarimetric WSR-88D: Description and application to an MCS. *Wea. Forecasting*, **24**, 730–748, doi:10.1175/2008WAF2222205.1.
- Phoenix, D. B., and C. R. Homeyer, 2021: Simulated impacts of tropopause-overshooting convection on the chemical composition of the upper troposphere and lower stratosphere. *J. Geophys. Res. Atmos.*, **126**, e2021JD034 568, doi:10.1029/2021JD034568.
- Ryzhkov, A. V., 2007: The impact of beam broadening on the quality of radar polarimetric data. *J. Atmos. Oceanic Technol.*, **24** (5), 729–744, doi:10.1175/JTECH2003.1.
- Ryzhkov, A. V., S. E. Giangrande, V. M. Melnikov, and T. J. Schuur, 2005a: Calibration issues of dual-polarization radar measurements. *J. Atmos. Oceanic Technol.*, **22**, 1138–1155.
- Ryzhkov, A. V., S. E. Giangrande, and T. J. Schuur, 2005b: Rainfall estimation with a polarimetric prototype of WSR-88D. *J. Appl. Meteor.*, **44**, 502–515.
- Ryzhkov, A. V., M. R. Kumjian, S. M. Ganson, and P. Zhang, 2013: Polarimetric radar characteristics of melting hail. Part II: Practical implications. *J. Appl. Meteor. Climatol.*, **in press**, doi:10.1175/JAMC-D-13-074.1.
- Ryzhkov, A. V., and D. S. Zrnić, 2007: Depolarization in ice crystals and its effect on radar polarimetric measurements. *J. Atmos. Oceanic Technol.*, **24** (7), 1256–1267, doi:10.1175/JTECH2034.1.
- Sandmæl, T. N., C. R. Homeyer, K. M. Bedka, J. M. Apke, J. R. Mecikalski, and K. Khlopenkov, 2019: Evaluating the ability of remote sensing observations to identify significantly severe and potentially tornadic storms. *J. Appl. Meteor. Climatol.*, **58**, 2569–2590, doi:10.1175/JAMC-D-18-0241.1.
- Schumacher, R. S., and K. L. Rasmussen, 2020: The formation, character and changing nature of mesoscale convective systems. *Nat Rev Earth Environ*, **1**, 300–314, doi:10.1038/s43017-020-0057-7.

- Starzec, M., C. R. Homeyer, and G. L. Mullendore, 2017: Storm Labeling in 3 Dimensions (SL3D): A volumetric radar echo and dual-polarization updraft classification algorithm. *Mon. Wea. Rev.*, **145**, 1127–1145, doi:10.1175/MWR-D-16-0089.1.
- Starzec, M., G. L. Mullendore, and C. R. Homeyer, 2020: Retrievals of convective detrainment heights using ground-based radar observations. *J. Geophys. Res. Atmos.*, **125**, doi:10.1029/2019JD031164.
- Stephens, G. L., and Coauthors, 2002: The CloudSat mission and the A-Train. a new dimension of space-based observations of clouds and precipitation. *Bull. Amer. Meteorol. Soc.*, **83**, 1771–1790, doi:10.1175/BAMS-83-12-1771.
- Thielen, J. E., and W. A. Gallus Jr., 2019: Influences of horizontal grid spacing and microphysics on WRF forecasts of convective morphology evolution for nocturnal MCSs in weakly forced environments. *Wea. Forecasting*, **34**, 1495–1517, doi:10.1175/WAF-D-18-0210.1.
- Tinney, E. N., and C. R. Homeyer, 2021: A 13-year trajectory-based analysis of convection-driven changes in upper troposphere lower stratosphere composition over the united states. *J. Geophys. Res. Atmos.*, **126**, e2020JD033 657, doi:10.1029/2020JD033657.
- Trapp, R. J., and C. A. Doswell, 2000: Radar data objective analysis. *J. Atmos. Oceanic Technol.*, **17**, 105–120.
- Wang, J., J. Fan, R. A. Houze, Jr., S. R. Brodzik, K. Zhang, G. J. Zhang, and P.-L. Ma, 2021: Using radar observations to evaluate 3-D radar echo structure simulated by the Energy Exascale Earth System Model (E3SM) version 1. *Geosci. Model Dev.*, **14**, 719–734, doi:10.5194/gmd-14-719-2021.
- Wang, J., R. A. Houze, Jr., J. Fan, S. R. Brodzik, Z. Feng, and J. C. Hardin, 2019: The detection of mesoscale convective systems by the GPM ku-band spaceborne radar. *J. Meteorol. Soc. Japan*, **97**, 1059–1073, doi: 10.2151/jmsj.2019-058.
- Wendt, N. A., and I. L. Jirak, 2021: An hourly climatology of operational MRMS MESH-diagnosed severe and significant hail with comparisons to *Storm Data* hail reports. *Wea. Forecasting*, **36**, 645–659, doi: 10.1175/WAF-D-20-0158.1.
- Winker, D. M., M. A. Vaughan, A. Omar, Y. Hu, K. A. Powell, Z. Liu, W. H. Hunt, and S. A. Young, 2009: Overview of the CALIPSO mission and CALIOP data processing algorithms. *J. Atmos. Oceanic Technol.*, **26**, 2310–2323, doi:10.1175/2009JTECHA1281.1.
- Zhang, J., K. Howard, and J. J. Gourley, 2005: Constructing three-dimensional multiple-radar reflectivity mosaics: Examples of convective storms and stratiform rain echoes. *J. Atmos. Oceanic Technol.*, **22**, 30–42.
- Zhang, J., S. Wang, and B. Clarke, 2004: WSR-88D reflectivity quality control using horizontal and vertical reflectivity structure. *11th Conf. on Aviation, Range, and Aerospace Meteorology*, Amer. Meteor. Soc., P5.4.
- Zhang, Y., J. Fan, T. Logan, Z. Li, and C. R. Homeyer, 2019: Wildfire impact on environmental thermodynamics and severe convective storms. *Geophys. Res. Lett.*, **46**, 10,082–10,093, doi:10.1029/2019GL084534.